



# Ligand-induced hollow MOF-derived carbon nanomaterials with abundant Fe species for efficient oxygen reduction

Lujiao Mao, Yongjie Ge\*, Dandan Chen, Yuandong Yang, Shaojie Xu, Jinhang Xue, Kuikui Xiao, Xuemei Zhou, Jinjie Qian\* and Zhi Yang\*

**ABSTRACT** The rational design and facile fabrication of cost-effective, efficient, and robust non-precious metal-based carbon nanomaterials are of great significance. Herein, under the control of temperature, the single-crystal-to-single-crystal transformation from MOF-5 to ZIF-8 *via* ligand exchange can be easily achieved with the intermediate and final structures of ZIF-8-M and ZIF-8-F, respectively. After pyrolysis of Fe-doped MOF (metal-organic framework) materials, Fe-ZIF-8-F-900 was obtained and featured large surface area, high degree of graphitization, a large number of carbon nanotubes, and highly active Fe species. All of these characteristics contribute to fast electron transfer and mass transport, resulting in a satisfactory oxygen reduction performance which is comparable to that of Pt/C, such as superior onset potential (0.982 V), limiting diffusion current density (5.41 mA cm<sup>-2</sup>), small Tafel slope (40.6 mV dec<sup>-1</sup>), and high current retention of 94.4% after 10 h. Furthermore, the experimental and simulation results both verify that the assembled zinc-air batteries possess excellent properties in practical applications. This study provides a rational design strategy for the development and preparation of high-efficiency and low-cost non-precious metal-based electrocatalysts, which further indicates new directions for energy-related practical applications.

**Keywords:** metal-organic framework, structural transformation, hollow morphology, carbon nanomaterial, oxygen reduction reaction

## INTRODUCTION

The consumption of traditional fossil fuels to generate energy will lead to a series of consequences and hazards, including atmospheric pollution and energy crises [1]. Therefore, we need to seek sustainable and green alternative fuels and enhance environmental protection and economic value. In this context, fuel cells and metal-air batteries experience rapid development and show application prospects owing to their environmental friendliness, high efficiency, and high energy density [2–7]. Although these devices can directly convert chemical energy into electricity through efficient and green redox reactions, their large reaction overpotential and sluggish reaction kinetics for the oxygen reduction reaction (ORR) at the cathode severely hinder their practical applications [8–10]. Generally, platinum-based carbon has been recognized as an excellent ORR catalyst with extraordinary catalytic activity, but its scarcity, high cost,

and poor durability limit its large-scale application [11,12]. Therefore, transition metal-based catalysts with cost-effectiveness, high efficiency, and robustness are considered to be promising alternatives which feature the rational design and convenient synthesis [13,14].

Porous metal-organic frameworks (MOFs) have been used to fabricate multifunctional transition metal-based nanomaterials [15–17]. Because of their large surface area, high porosity, and numerous active sites, MOF materials and their derivatives can be widely applied in various research fields [18–20]. Recently, hollow-structured MOFs have been receiving extensive attention because they possess large pore volume and abundant active sites, thus facilitating mass transport [21,22]. Generally, researchers have employed templates to prepare hollow MOF-derived nanomaterials where hard templates include silicon microspheres and polystyrene [23], while soft templates include micelles and vesicles [24]. Although the size, morphology, and structure can be precisely controlled by the template method, it is difficult, complicated, and expensive. Whether MOF materials could be *in situ* transformed into hollow morphology for efficient catalysis based on their composition and structural characteristics needs to be explored.

Alternatively, highly active and selective metal-nitrogen (M-N<sub>x</sub>) carbons that mimic biological nanoenzymes are prepared through the decomposition of MOFs [25,26]. The obtained MOF-derived carbon nanomaterials have the advantages of exposed metal-rich nanoparticles (NPs) and M-N<sub>x</sub> sites, which can enhance electrochemical properties [27,28]. With the reasonable selection of self-sacrificial templates, these porous N-containing MOF materials that intrinsically have numerous N sites can effectively disperse and anchor transition metal ions [29]. After carbonization, the facile formation of M-N<sub>x</sub> sites and ultrafine metal particles leads to superior electrocatalytic ORR performance. Meanwhile, previous experiments and theories have confirmed that doping transition metals into N-rich MOF precursors through carbonization can effectively promote ORR catalytic activity [30]. Therefore, the addition of transition metal ions to *in-situ*-formed hollow-structured MOFs is highly challenging and expected to regulate the components and structures of MOF-derived electrocatalysts, as well as their electrochemical properties.

In this work, we have exploited the single-crystal-to-single-crystal (SCSC) transformation method to achieve structural transformation from the initial MOF-5 cubes to the hollow ZIF-8-F (Fig. 1a). Through competitive ligand coordination, the

Key Laboratory of Carbon Materials of Zhejiang Province, College of Chemistry and Materials Engineering, Wenzhou University, Wenzhou 325035, China  
\* Corresponding authors (emails: [geyongjie1220@126.com](mailto:geyongjie1220@126.com) (Ge Y); [yangzhi@wzu.edu.cn](mailto:yangzhi@wzu.edu.cn) (Yang Z); [jinjieqian@wzu.edu.cn](mailto:jinjieqian@wzu.edu.cn) (Qian J))

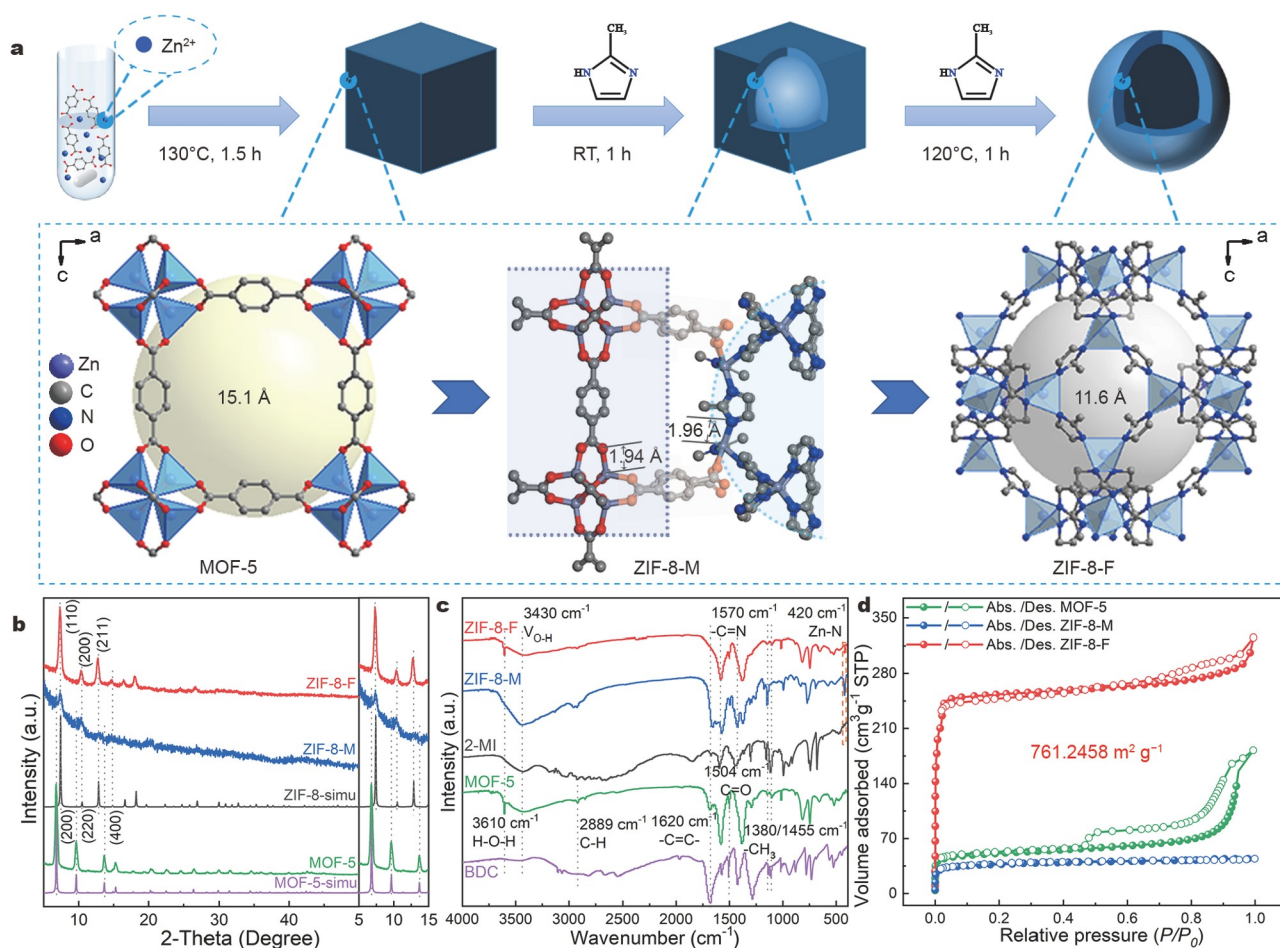


**Figure 1** (a) Schematic representation of the structural conversion from MOF-5 to ZIF-8; (b) PXRD patterns; (c) FT-IR spectra; (d) N<sub>2</sub> isotherms.

ligand exchange between 1,4-benzenedicarboxylate (BDC<sup>2-</sup>) in MOF-5 and 2-methylimidazole (MI) in ZIF-8, the cleavage of the weak coordination bonds, and the continuous generation of strong bonds can yield a hollow nanostructure. When ferric salts are introduced, Fe(III) ions are uniformly dispersed in the hollow MOF micropores and large internal cavities and form strong chemical interactions at the exposed N site. After pyrolysis, porous N-doped Fe-ZIF-8-F-900 with multiwalled carbon nanotubes and abundant Fe species can be conveniently obtained. Meanwhile, the well-preserved hollow carbon can increase the pore volume to expose the active substances and improve the charge transport. Fe-ZIF-8-F-900 exhibits a satisfactory ORR performance in terms of an onset potential of 0.982 V, half-wave potential of 0.865 V, and limiting diffusion current density of 5.41 mA cm<sup>-2</sup>. The zinc-air batteries (ZABs) based on Fe-ZIF-8-F-900 also show excellent performance.

## RESULTS AND DISCUSSION

In Fig. 1a, the single-crystal structure of MOF-5 consists of typical [Zn<sub>4</sub>O]<sup>6+</sup> building units and BDC<sup>2-</sup> ligands, whereas each Zn(II) ion in ZIF-8 is four-coordinated with N atoms of adjacent MI linkers. Because of the similar coordination environment between the two MOFs, SCSC transformation under certain conditions could be most likely achieved (Figs S1 and S2 and Tables S1 and S2) [31].

Therefore, with the dispersion of these prefabricated MOF-5

nanocrystals in dimethyl formamide (DMF) solution with MI molecules, Zn–O and Zn–N bonds will exert competitive coordination at the interface of MOF precursors. Notably, the Zn–O bonds are continuously decomposed with the generation of the Zn–N bonds, resulting in a more thermodynamically stable ZIF-8 structure (Fig. S3) [32,33]. During the process, an interesting intermediate called ZIF-8-medium (ZIF-8-M) containing both MOF-5 and ZIF-8 was detected. The product that is completely converted at a high temperature is denoted as ZIF-8-final (ZIF-8-F; more details are provided in the experimental part in the Supplementary information). In Fig. 1b, powder X-ray diffraction (PXRD) analysis shows that the obtained MOF-5 microcubes are highly crystalline with narrow diffraction peaks, and the simulation results show that ZIF-8-F has high purity and crystallinity. Notably, ZIF-8-M exhibits two sets of peaks for both MOFs, which indicates the successful SCSC conversion. Meanwhile, the Fourier transformed infrared (FT-IR) spectra reveal obvious signals at 1570 cm<sup>-1</sup> (C=N stretching) and 420 cm<sup>-1</sup> (Zn–N stretching) that further confirm the formation of heterostructures (Fig. 1c) [34]. Furthermore, the N<sub>2</sub> sorption curves of all involved MOFs exhibit hysteresis loops (Fig. 1d and Fig. S4), and the Brunauer-Emmett-Teller (BET) specific surface areas of MOF-5, ZIF-8-M, and ZIF-8-F are calculated to be 162.0, 115.2, and 761.2 m<sup>2</sup> g<sup>-1</sup>, respectively, and their total pore volumes are 0.24, 0.07, and 0.47 cm<sup>3</sup> g<sup>-1</sup>, respectively (Table S3). In this case, ZIF-8-F has a larger specific surface area than MOF-

5 and ZIF-8-M because of its unique hollow nanostructure.

The scanning electron microscopy (SEM) image of the initial MOF-5 shows a regular cubic shape with a uniform size of approximately 1  $\mu\text{m}$  (Fig. 2a). Notably, a light-dark junction can be observed in Fig. 2b and Fig. S5, indicating that the core-shell structure has been formed. The transmission electron microscopy (TEM) image shows that the outer wall of ZIF-8-M maintains the cubic morphology of the MOF-5 precursor with slight shrinkage inward, whereas the interior is a solid structure,

which indicates that the SCSC transformation reaction starts from the inside (Fig. 2c). Furthermore, the corresponding element mapping and energy-dispersive X-ray spectrum (EDS) reveal the uniform distribution of Zn, C, N, and O on the entire surface (Fig. 2d-f).

When MI is added at 120°C, many small rough NPs are anchored on the surface. The obtained ZIF-8-F has a hollow nanostructure with a slightly rough surface, dense shell, and uniform thickness (Fig. 2g). In Fig. 2h and Fig. S6, the typical

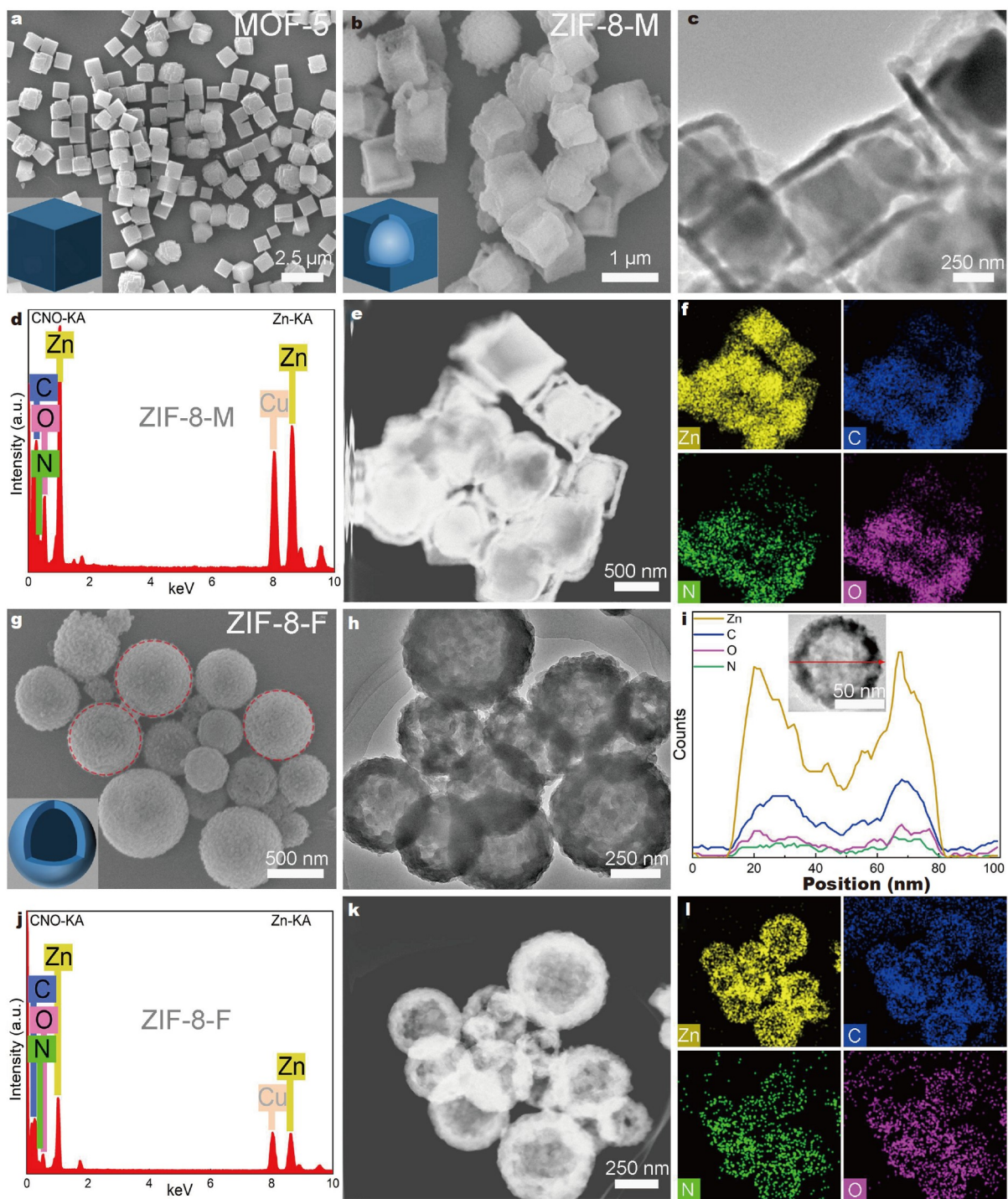


**Figure 2** (a) SEM image of the MOF-5 precursor; SEM, TEM, and EDS images and element mappings of ZIF-8-M (b-f) and ZIF-8-F (g, h, j-l); (i) compositional line profile for hollow ZIF-8-F.

hollow structure with a brighter hollow core and a darker shell with an average thickness of approximately 200 nm are consistent with the analysis. Furthermore, a single sphere-like particle is randomly selected for line scanning to illustrate that Zn, C, N, and O in the core layer are fewer than that on the outer shell, confirming the hollow morphology shown in Fig. 2i. Finally, the uniform distribution of Zn, C, N, and O on the outer shell was also detected by EDS and element mapping (Fig. 2j–l).

Notably, Fe-based active sites can be effectively generated after Fe doping in N-rich Zn-MOFs, whereas single Fe-N<sub>x</sub> atoms exhibit a superior electronic structure during the catalytic reaction (Fig. S7) [27]. According to the thermogravimetric analysis (TGA) curves shown in Fig. S8, the process involves solvent volatilization and precursor carbonization and tends to be thermally stable with nearly no weight loss after 900°C.

Three types of Fe-doped carbon nanomaterials, namely, Fe-MOF-5-900, Fe-ZIF-8-M-900, and Fe-ZIF-8-F-900, were conveniently obtained. In Figs S9 and S10, Fe-MOF-5-900 well retains its cubic shape, whereas Fe-ZIF-8-M-900 exhibits slight shrinkage. The coexistence of Zn, Fe, C, N, and O can also be

detected in both EDS curves and element mappings. In the element mappings, a large number of carbon nanotubes can be observed for Fe-ZIF-8-F-900, which could speed up electron transport for efficient electrocatalysis (Fig. 3a and Fig. S11) [35]. The high-resolution TEM (HR-TEM) images show some noticeable lattice fringes of 0.346 nm ascribed to the (002) plane of graphite and 0.203 nm ascribed to the (110) plane of metallic iron (Fig. 3b, c). The high-angle annular dark field scanning TEM (HAADF-STEM) images, element mappings, and EDS curve verify the uniform distribution of constituent elements in Fig. 3d–f and Table S4. In this case, a nearly negligible amount of Zn can be interpreted as most Zn species having been volatilized (Fig. S12). In Fig. 3g, the Raman spectra show that the intensity ratio of D band and G band ( $I_D/I_G$ ) of Fe-ZIF-8-F-900 (0.9649) is smaller than those of Fe-MOF-5-900 (0.9935) and Fe-ZIF-8-M-900 (1.0246), indicating that Fe-ZIF-8-F-900 has a higher graphitization degree. In Fig. 3h, the PXRD patterns show the obvious characteristic peaks at 43.7° and 44.7°, which can be attributed to the Fe<sub>3</sub>C (111) and metallic Fe (110) planes, respectively. Moreover, its Type IV N<sub>2</sub> isotherm shows that the

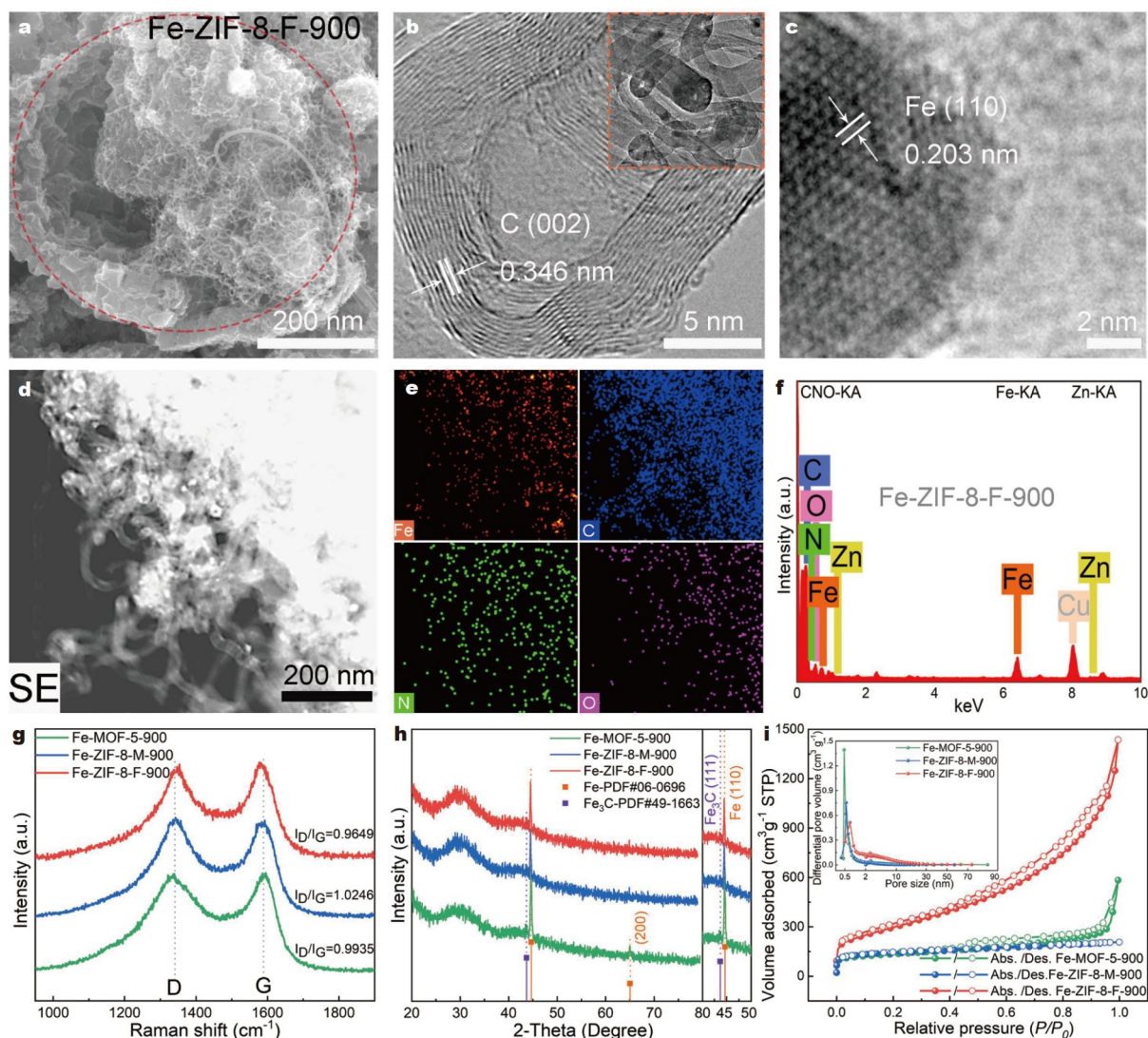


**Figure 3** (a–d) SEM, TEM, HR-TEM, and HAADF-STEM images of Fe-ZIF-8-F-900; (e, f) element mappings and EDS curve of Fe-ZIF-8-F-900; (g) Raman spectra, (h) PXRD patterns, and (i) N<sub>2</sub> isotherms of MOF-derived carbon nanomaterials.

specific surface area of Fe-ZIF-8-F-900 reaches  $1073 \text{ m}^2 \text{ g}^{-1}$ , and the pore size distribution confirms the formation of micropores/mesopores (Fig. 3i). Overall, Fe-ZIF-8-F-900 has a large number of carbon nanotubes, large specific surface area, high graphitization degree, and hierarchical pores, which are conducive to promoting electron transfer and mass transport.

X-ray photoelectron spectroscopy (XPS) was further performed to probe their electronic structure and surface information. In Fig. 4a, the full survey spectra show the discernible signals of C 1s, N 1s, and O 1s and the subtle signals of Fe 2p and Zn 2p for all involved carbon samples. The high-resolution Zn 2p spectra show that most of the Zn species have been removed after carbonization (Fig. S13) [36]. The high-resolution C 1s spectra can be fitted into five separate peaks with C=C  $\text{sp}^2$  (284.5 eV), C-C  $\text{sp}^3$  (286.0 eV), C-O/C-N (287.3 eV), C=O/C=N (288.8 eV), and O=C-O (290.3 eV), as shown in Fig. 4b.

The deconvoluted N 1s spectra of Fe-ZIF-8-M/F-900 can be divided into four subpeaks, namely, pyridinic N (398.3 eV), pyrrolic N (399.5 eV), graphitic N (400.6 eV), and oxidized N (403.9 eV) (Fig. 4c). Notably, pyridinic and graphitic N are regarded as the main active components for the efficient adsorption and reduction of oxygen intermediates [37]. The slightly shifted positions of the N peaks are attributed to the fact that Fe-ZIF-8-M-900 is in the intermediate state whose Zn-N bond is not fully transferred. Meanwhile, Fe-ZIF-8-F-900 shows an extra weak peak at 397.6 eV from the *in-situ*-formed Fe-N<sub>x</sub>

species, providing more active sites for efficient catalysis. For the O 1s spectra, two typical peaks of C-O (532.9 eV) and M-O (531.0 eV) are detected (Fig. S14). Moreover, for the high-resolution Fe 2p spectra, two subpeaks at 714.0 and 727.1 eV can be reasonably attributed to the Fe-N<sub>x</sub> species. Meanwhile, for the Fe 2p<sub>3/2</sub> (710.6 eV) and Fe 2p<sub>1/2</sub> (723.2 eV) spectra, two satellite peaks at 718.0 and 730.5 eV can be detected. Furthermore, a negatively shifted binding energy of 0.2 eV in Fe 2p<sub>3/2</sub> can be detected in Fe-ZIF-8-F-900 because of a more N-donating effect [38]. Thus, the obtained Fe-ZIF-8-F-900 is equipped with abundant graphitic carbon and Fe-N<sub>x</sub> sites, which facilitate electron transport to enhance electrocatalytic ORR performance.

Because of the large specific surface area, high graphitization degree, and abundant Fe species, excellent ORR performance is expected. First, electrochemical activity was evaluated through cyclic voltammetry (CV) measurements using commercial 20 wt% Pt/C. Prominent oxygen reduction peaks were detected in an O<sub>2</sub>-saturated 0.1 mol L<sup>-1</sup> KOH solution, whereas oxygen reduction peaks were not obvious in the N<sub>2</sub>-saturated 0.1 mol L<sup>-1</sup> KOH solution. In Fig. 5a and Fig. S15, Fe-ZIF-8-F-900 exhibits one cathodic peak at 0.90 V close to Pt/C (0.93 V), higher than that of Fe-ZIF-8-M-900 (0.85 V) and Fe-MOF-5-900 (0.80 V). Meanwhile, the rotating ring-disk electrode (RRDE) method reveals a superior onset potential ( $E_{\text{onset}} = 0.982 \text{ V}$ ), half-wave potential ( $E_{1/2} = 0.865 \text{ V}$ ), and limiting diffusion current density ( $J_L = 5.41 \text{ mA cm}^{-2}$ ) for Fe-ZIF-8-F-900, which is com-

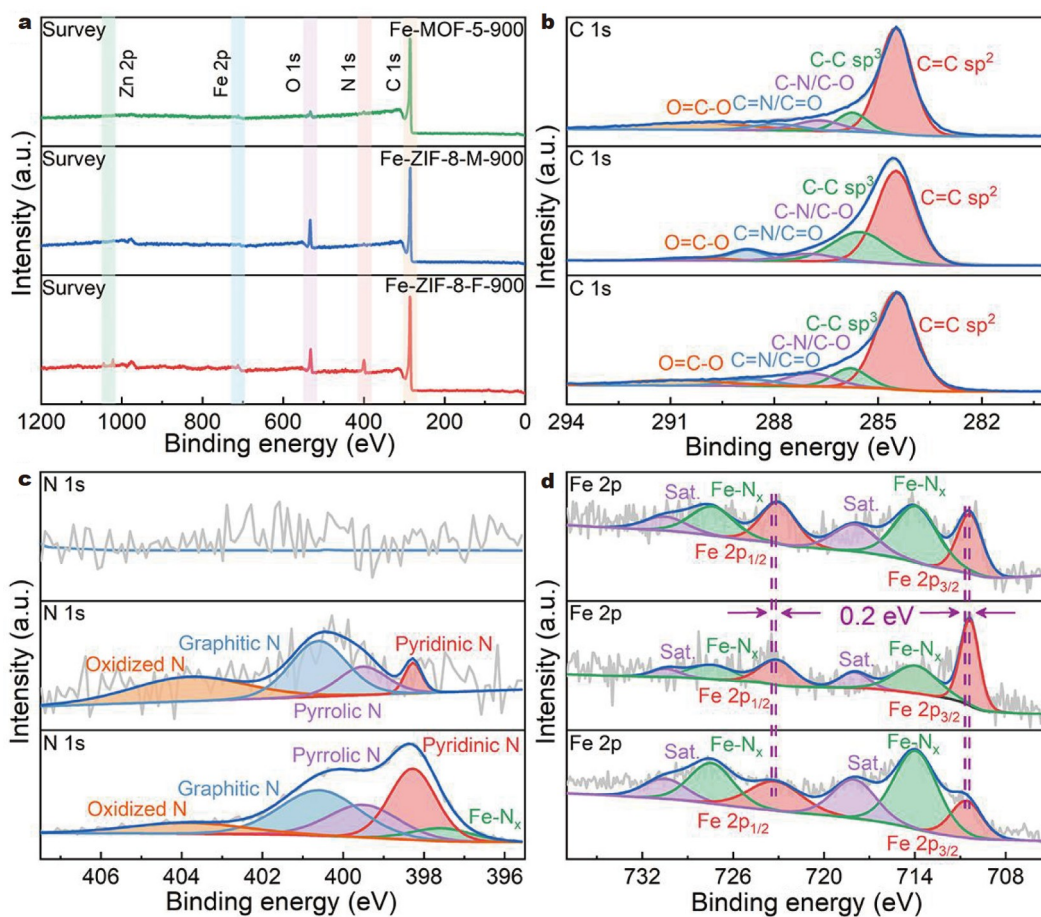


**Figure 4** (a) Full survey XPS spectra and the deconvoluted spectra of (b) C 1s, (c) N 1s, and (d) Fe 2p (from top to bottom: Fe-MOF-5-900, Fe-ZIF-8-M-900, Fe-ZIF-8-F-900).

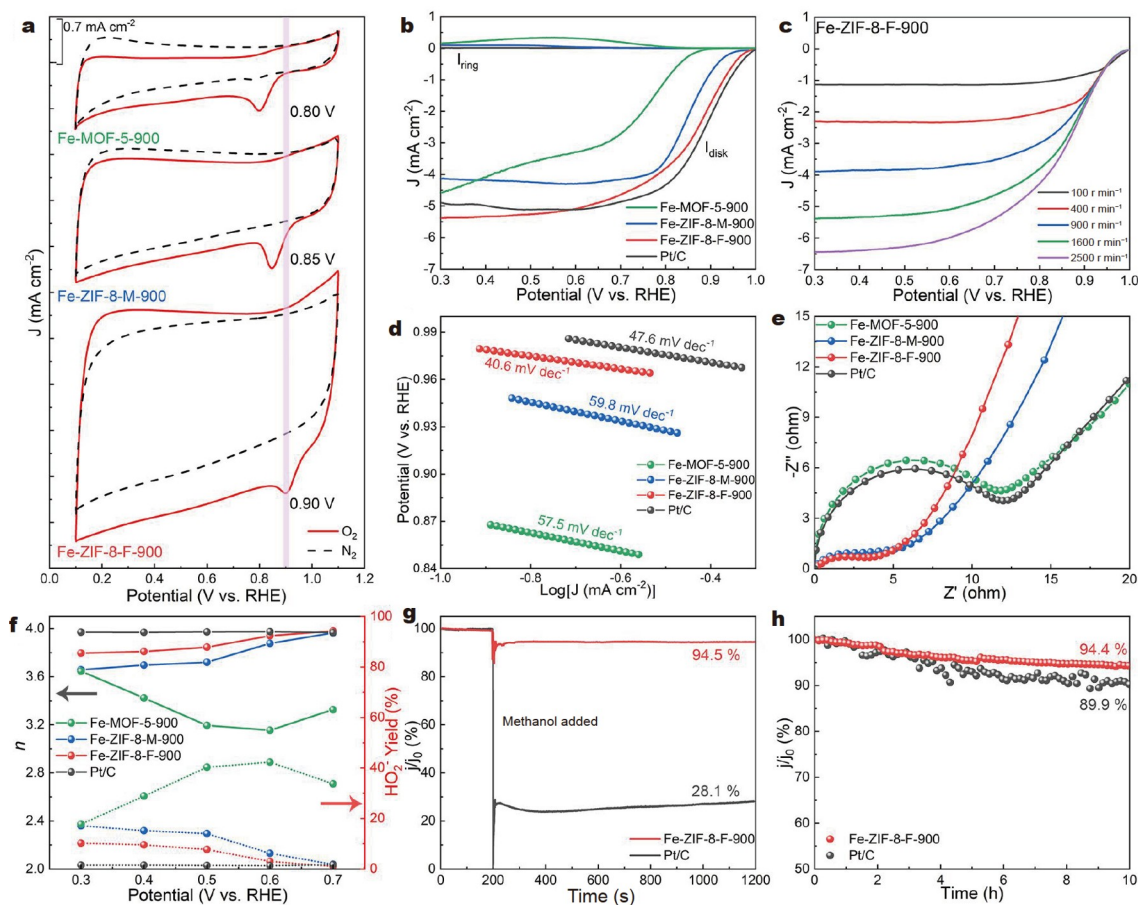


**Figure 5** (a) CV and (b) LSV curves at  $1600 \text{ r min}^{-1}$ ; (c) LSV curves with various rotating speeds for Fe-ZIF-8-F-900; (d) Tafel slopes; (e) EIS plots; (f)  $n$  (top) and  $\text{HO}_2^-$  yield (bottom); (g, h) anti-MeOH and stability evaluation.

parable to Pt/C ( $E_{\text{onset}} = 0.992 \text{ V}$ ,  $E_{1/2} = 0.884 \text{ V}$ , and  $J_L = 5.24 \text{ mA cm}^{-2}$ ) and competitive to recently reported catalysts (Fig. 5b and Table S5). Moreover, Fig. 5c and Figs S16, S17 show the linear sweep voltammetry (LSV) curves at different rotating speeds, and the corresponding Koutechy-Levich plots reflect the first-order reaction kinetics [39].

The corresponding Tafel slopes are 40.6, 57.5, 59.8, and  $47.6 \text{ mV dec}^{-1}$  for Fe-ZIF-8-F-900, Fe-MOF-5-900, Fe-ZIF-8-M-900, and Pt/C, respectively, indicating that Fe-ZIF-8-F-900 intrinsically has excellent reaction kinetics (Fig. 5d). Electrochemical impedance spectroscopy reveals the lowest charge transfer resistance ( $R_{\text{ct}}$ ) of  $3.9 \Omega$  for Fe-ZIF-8-F-900 (Fig. 5e and Table S6). Alternatively, the electrochemical surface area can be evaluated using the double-layer capacitance ( $C_{\text{dl}}$ ) based on the CV curves, in which Fe-ZIF-8-F-900 has a high  $C_{\text{dl}}$  value of  $13.9 \text{ mF cm}^{-2}$  (Figs S18 and S19). In Fig. 5f, the average number of electrons ( $n$ ) of Fe-ZIF-8-F-900 is calculated to be 3.8 (close to 4) with a low  $\text{HO}_2^-$  yield, indicating its quasi-4e pathway. When  $3.0 \text{ mol L}^{-1}$  methanol is added, Fe-ZIF-8-F-900 remains stable and has a high current retention rate of 94.5%, whereas Pt/C shows poor resistance (28.1%; Fig. 5g). Meanwhile, the current densities of both materials decrease with time, but the durability of Fe-ZIF-8-F-900 (94.4%) is better than that of Pt/C (89.9%) after 10 h (Fig. 5h and Fig. S20).

Fe-ZIF-8-F-900 was applied to assemble ZABs for practical applications. As shown in Fig. 6a, the cathode is made of catalyst-supported carbon paper, and the anode is a polished Zn

plate in a  $6.0 \text{ mol L}^{-1}$  KOH solution. Notably, the Zn plate will be electrochemically oxidized into  $[\text{Zn}(\text{OH})_4]^{2-}$  ions, whereas the supported catalyst undergoes a rigorous oxygen reduction at the interface during the discharge process [40]. Thus, the ZAB device was well fabricated based on our catalyst, as well as Pt/C, and the ZAB device based on Fe-ZIF-8-F-900 has an open-circuit voltage (OCV) of 1.49 V, which is comparable to that of Pt/C (1.50 V; Fig. 6b).

The two connected ZABs are further employed in series to successfully light a light emitting diode (LED) screen and verify its practicability. Fig. 6c shows that Fe-ZIF-8-F-900 has a maximum power density of  $102.8 \text{ mW cm}^{-2}$ , which is close to that of Pt/C ( $103.4 \text{ mW cm}^{-2}$ ). Herein, the Fe-ZIF-8-F-900-based ZAB exhibits a competitive performance to the Pt/C-based one, and its specific capacity at  $10 \text{ mA cm}^{-2}$  is  $710.3 \text{ mA h g}^{-1}$  after 8 h, which is higher than that of Pt/C ( $701.8 \text{ mA h g}^{-1}$ ; Fig. 6d and Table S7). In this case, the excellent electrocatalytic property stems from the high N content and Fe- $\text{N}_x$  active components, and the large specific surface area can effectively promote the diffusion and exchange of gas molecules [41]. Meanwhile, these *in-situ*-grown carbon nanotubes could facilitate electron transfer and mass transport, thereby enhancing the ORR reactivity and durability.

To simplify the theoretical calculations, only the role of Fe- $\text{N}_x$  sites in promoting electrocatalytic ORR was investigated to reveal the adsorption energy of  $\text{O}_2$  for these MOF-derived carbon nanocatalysts. Given that Fe- $\text{N}_x$  species usually serve as the

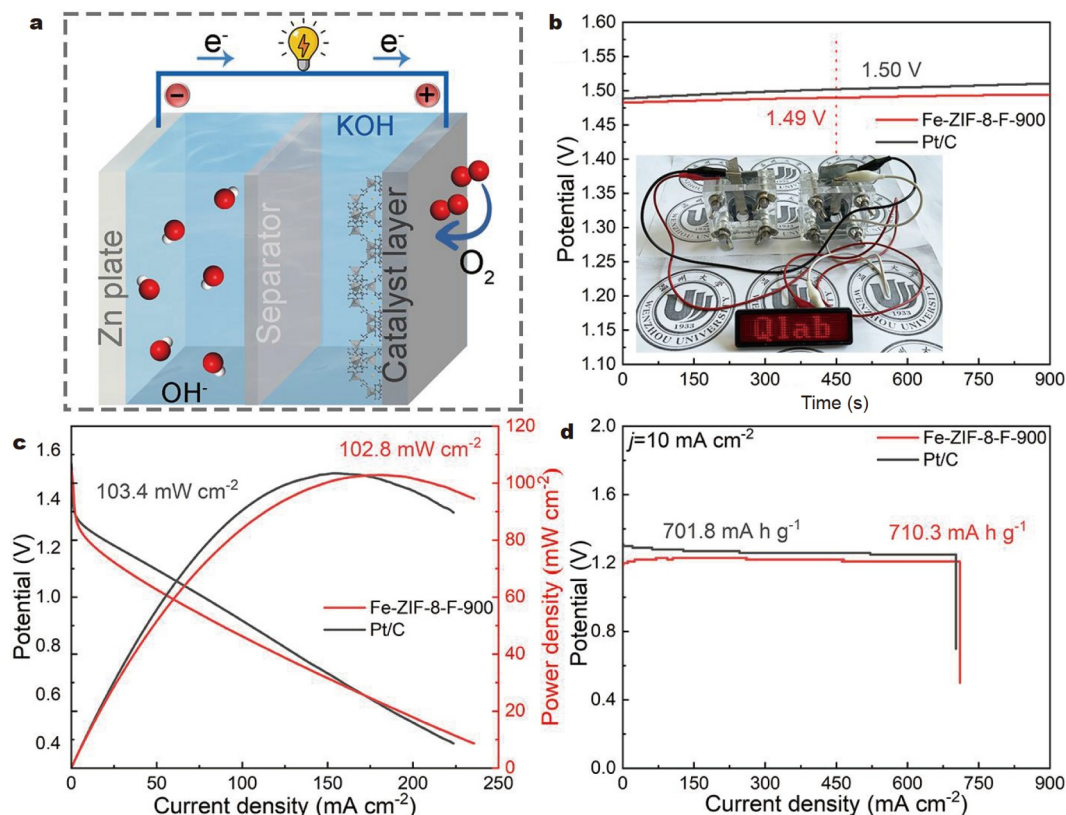


**Figure 6** (a) Diagram of an assembled ZAB; (b) OCV profiles (the inset shows two ZABs in series); (c) polarization and power density curves; (d) galvanostatic discharge curves at  $10 \text{ mA cm}^{-2}$  of Fe-ZIF-8-F-900-based and Pt/C-based ZABs.

most effective active sites, the selection of the thermodynamically stable Fe-N<sub>4</sub> center as the standard model is rational.

In this case, two types of carbon nanostructures, namely, Fe-doped graphene (G-Fe) for pure Fe-MOF-5-900 and graphene with Fe-N<sub>x</sub> sites (G-Fe-N) for Fe-ZIF-8-F-900, were constructed. According to the calculated adsorption energy data ( $E_a$ ), the O<sub>2</sub> adsorption capacity of G-Fe-N ( $-2.688 \text{ eV}$ ) is higher than that of G-Fe ( $-2.671 \text{ eV}$ ) (Fig. 7a, Fig. S21 and Table S8). Alternatively, the partial density of states (PDOS) diagram shown in Fig. 7b indicates that G-Fe-N exhibits a notably broadened energy through valence hybridization compared with pure O<sub>2</sub>. Part of the charge will be transferred from O<sub>2</sub> molecules to G-Fe-N, and the presence of Fe-N<sub>x</sub> sites will enhance the adsorption capacity of O<sub>2</sub>. Finally, the detailed 4e pathway at the Fe-N<sub>4</sub> center in the ORR process is illustrated in Fig. 7c. First, O<sub>2</sub> adsorbs on the Fe atom on the catalyst surface to form \*O<sub>2</sub>, which then reacts with one electron to form \*OOH and retains the transition state of O\* after the decomposition of OOH\*. Afterward, the dissociated OH\* adsorbs on the central atom. Finally, after the OH<sup>-</sup> group escapes, the ORR process is completed [42,43]. Overall, both the experimental and computational data indicate that the obtained Fe-ZIF-8-F-900 preferentially adsorbs and reduces O<sub>2</sub> molecules and the synergistic effect of Fe-N<sub>x</sub> strongly promotes the ORR response.

## CONCLUSION

In summary, Fe-ZIF-8-F-900, one type of hollow-structured carbon nanomaterial with carbon nanotubes and Fe species, has

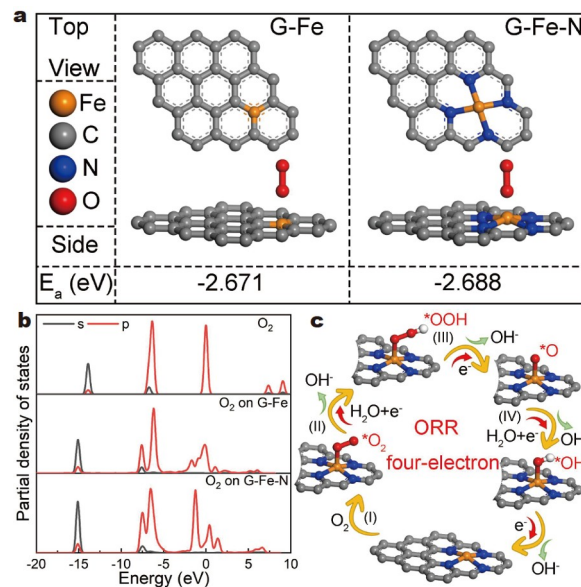


**Figure 7** (a) Geometrically optimized nanostructures; (b) PDOS curves after O<sub>2</sub> adsorption; (c) ORR mechanism on the Fe-N<sub>4</sub> site (red/white: O/H atoms).

been successfully prepared by the ligand-induced SCSC transformation method followed by high-temperature pyrolysis. Because of the large specific surface area, high graphitization degree, and a large number of micropores/mesopores, a satisfactory electrocatalytic ORR performance of these MOF-derived

carbons can be conveniently achieved. In this case, the large surface area can effectively promote the diffusion and exchange of gas molecules, while the high graphitization degree is beneficial to rapid electron transport, thereby enhancing the ORR reactivity and durability. We have further used Fe-ZIF-8-F-900, which exhibits a large OCV value, high power density, and large specific capacity, to assemble ZABs for practical applications. Moreover, the excellent electrocatalytic property is validated by theoretical calculations. Finally, this study will provide a rational design strategy for ligand-induced hollow MOF-derived carbon nanomaterials with specific morphology and further shed light on new directions for energy-related practical applications.

Received 3 November 2022; accepted 25 December 2022;  
published online 22 March 2023

- Jacobson MZ. Review of solutions to global warming, air pollution, and energy security. *Energy Environ Sci*, 2009, 2: 148–173
- Wang Q, Feng Q, Lei Y, *et al.* Quasi-solid-state Zn-air batteries with an atomically dispersed cobalt electrocatalyst and organohydrogel electrolyte. *Nat Commun*, 2022, 13: 3689
- Najam T, Shah SSA, Ibraheem S, *et al.* Single-atom catalysis for zinc-air/O<sub>2</sub> batteries, water electrolyzers and fuel cells applications. *Energy Storage Mater*, 2022, 45: 504–540
- Ren JT, Ying YD, Liu YP, *et al.* Charge redistribution caused by sulfur doping of bimetal FeCo phosphides supported on heteroatoms-doped graphene for Zn-air batteries with stable cycling. *J Energy Chem*, 2022, 71: 619–630
- Wang P, Chen D, Pan J, *et al.* Wrinkled reduced graphene oxide supported nano Ag<sub>2</sub>Bi<sub>2</sub>O<sub>5</sub> rods as greatly enhanced catalyst for zinc-air battery. *J Electrochem Soc*, 2019, 166: A968–A974
- Sun Y, Yang M, Pan J, *et al.* Manganese dioxide-supported silver bismuthate as an efficient electrocatalyst for oxygen reduction reaction in zinc-oxygen batteries. *Electrochim Acta*, 2016, 197: 68–76
- Zeng X, Pan J, Sun Y. Preparation of Ag<sub>2</sub>Bi<sub>2</sub>O<sub>5</sub>/MnO<sub>2</sub> corn/cob like nano material as a superior catalyst for oxygen reduction reaction in alkaline solution. *Catalysts*, 2017, 7: 379
- Yu J, Dai Y, Zhang Z, *et al.* Tailoring structural properties of carbon *via* implanting optimal Co nanoparticles in N-rich carbon cages toward high-efficiency oxygen electrocatalysis for rechargeable Zn-air batteries. *Carbon Energy*, 2022, 4: 576–585
- Wang T, Zhang Y, Huang B, *et al.* Enhancing oxygen reduction electrocatalysis by tuning interfacial hydrogen bonds. *Nat Catal*, 2021, 4: 753–762
- Choi S, Do HW, Jin D, *et al.* Revisiting the role of the triple-phase boundary in promoting the oxygen reduction reaction in aluminum-air batteries. *Adv Funct Mater*, 2021, 31: 2101720
- Liu M, Zhao Z, Duan X, *et al.* Nanoscale structure design for high-performance Pt-based ORR catalysts. *Adv Mater*, 2019, 31: 1802234
- Zhu X, Tan X, Wu KH, *et al.* Intrinsic ORR activity enhancement of Pt atomic sites by engineering the d-band center *via* local coordination tuning. *Angew Chem Int Ed*, 2021, 60: 21911–21917
- Wang X, Dong A, Zhu Z, *et al.* Surfactant-mediated morphological evolution of MnCo Prussian blue structures. *Small*, 2020, 16: 2004614
- Yan Y, Wang P, Lin J, *et al.* Modification strategies on transition metal-based electrocatalysts for efficient water splitting. *J Energy Chem*, 2021, 58: 446–462
- Xue Y, Guo Y, Zhang Q, *et al.* MOF-derived Co and Fe species loaded on N-doped carbon networks as efficient oxygen electrocatalysts for Zn-air batteries. *Nano-Micro Lett*, 2022, 14: 162
- Zhao T, Wu H, Wen X, *et al.* Recent advances in MOFs/MOF derived nanomaterials toward high-efficiency aqueous zinc ion batteries. *Coord Chem Rev*, 2022, 468: 214642
- Kong F, Cui X, Huang Y, *et al.* N-doped carbon electrocatalyst: Marked ORR activity in acidic media without the contribution from metal sites? *Angew Chem Int Ed*, 2022, 61: e202116290
- Chen Z, Chen Z, Farha OK, *et al.* Mechanistic insights into nanoparticle formation from bimetallic metal-organic frameworks. *J Am Chem Soc*, 2021, 143: 8976–8980
- Wang Y, Pan Y, Zhu L, *et al.* Solvent-free assembly of Co/Fe-containing MOFs derived N-doped mesoporous carbon nanosheets for ORR and HER. *Carbon*, 2019, 146: 671–679
- Lu XF, Xia BY, Zang SQ, *et al.* Metal-organic frameworks based electrocatalysts for the oxygen reduction reaction. *Angew Chem Int Ed*, 2020, 59: 4634–4650
- Yang H, Wang X. Secondary-component incorporated hollow MOFs and derivatives for catalytic and energy-related applications. *Adv Mater*, 2019, 31: 1800743
- Li T, Ding B, Malgras V, *et al.* Hollow carbon architectures with mesoporous shells *via* self-sacrificial templating strategy using metal-organic frameworks. *Chem Eng J*, 2021, 420: 127635
- Sun Q, Ding J, Chen D, *et al.* Silica-templated metal organic framework-derived hierarchically porous cobalt oxide in nitrogen-doped carbon nanomaterials for electrochemical glucose sensing. *ChemElectroChem*, 2021, 8: 812–818
- Fan W, Liu L, Zhao H. Co-assembly of patchy polymeric micelles and protein molecules. *Angew Chem Int Ed*, 2017, 56: 8844–8848
- Miao Z, Wang X, Zhao Z, *et al.* Improving the stability of non-noble-metal M–N–C catalysts for proton-exchange-membrane fuel cells through M–N bond length and coordination regulation. *Adv Mater*, 2021, 33: 2006613
- Garg R, Sahoo L, Kaur K, *et al.* Single-step insertion of M–N<sub>x</sub> moieties in commercial carbon for sustainable bifunctional electrocatalysis: Mapping insertion capacity, mass loss, and carbon reconstruction. *Carbon*, 2022, 196: 1001–1011
- Sun Q, Zhu K, Ji X, *et al.* MOF-derived three-dimensional ordered porous carbon nanomaterial for efficient alkaline zinc-air batteries. *Sci China Mater*, 2022, 65: 1453–1462
- Huang Q, Xu Y, Guo Y, *et al.* Highly graphitized N-doped carbon nanosheets from 2-dimensional coordination polymers for efficient metal-air batteries. *Carbon*, 2022, 188: 135–145
- Zhang W, Xu CH, Zheng H, *et al.* Oxygen-rich cobalt-nitrogen-carbon porous nanosheets for bifunctional oxygen electrocatalysis. *Adv Funct Mater*, 2022, 32: 2200763
- Liu J, Zhang H, Meng J, *et al.* A “MOFs plus ZIFs” strategy toward ultrafine Co nanodots confined into superficial N-doped carbon nanowires for efficient oxygen reduction. *ACS Appl Mater Interfaces*, 2020, 12: 54545–54552
- Yang Y, Huang Q, Sun Q, *et al.* Fe-induced coordination environment regulation in MOF-derived carbon materials for oxygen reduction. *ACS Sustain Chem Eng*, 2022, 10: 8641–8649
- Xing J, Schweighauser L, Okada S, *et al.* Atomistic structures and dynamics of prenucleation clusters in MOF-2 and MOF-5 syntheses. *Nat Commun*, 2019, 10: 3608
- Low JJ, Benin AI, Jakubczak P, *et al.* Virtual high throughput screening confirmed experimentally: Porous coordination polymer hydration. *J Am Chem Soc*, 2009, 131: 15834–15842
- Fan S, Wang S, Wang X, *et al.* Photogated proton conductivity of ZIF-8 membranes co-modified with graphene quantum dots and polystyrene sulfonate. *Sci China Mater*, 2021, 64: 1997–2007
- Xia D, Yang X, Xie L, *et al.* Direct growth of carbon nanotubes doped with single atomic Fe–N<sub>4</sub> active sites and neighboring graphitic nitrogen for efficient and stable oxygen reduction electrocatalysis. *Adv Funct Mater*, 2019, 29: 1906174
- Huang Y, Liu K, Kan S, *et al.* Highly dispersed Fe–N<sub>x</sub> active sites on graphitic-N dominated porous carbon for synergetic catalysis of oxygen reduction reaction. *Carbon*, 2021, 171: 1–9
- Wang X, Jia Y, Mao X, *et al.* A directional synthesis for topological defect in carbon. *Chem*, 2020, 6: 2009–2023
- Liu Y, He S, Huang B, *et al.* Influence of different Fe doping strategies on modulating active sites and oxygen reduction reaction performance of Fe, N-doped carbonaceous catalysts. *J Energy Chem*, 2022, 70: 511–520
- Liang Y, Li Y, Wang H, *et al.* Co<sub>3</sub>O<sub>4</sub> nanocrystals on graphene as a synergistic catalyst for oxygen reduction reaction. *Nat Mater*, 2011, 10: 780–786

- 40 Li Z, Ganapathy S, Xu Y, *et al.* Mechanistic insight into the electrochemical performance of Zn/VO<sub>2</sub> batteries with an aqueous ZnSO<sub>4</sub> electrolyte. *Adv Energy Mater*, 2019, 9: 1900237
- 41 Matsumoto K, Onoda A, Kitano T, *et al.* Thermally controlled construction of Fe-N<sub>x</sub> active sites on the edge of a graphene nanoribbon for an electrocatalytic oxygen reduction reaction. *ACS Appl Mater Interfaces*, 2021, 13: 15101–15112
- 42 Chen Y, Ji S, Zhao S, *et al.* Enhanced oxygen reduction with single-atomic-site iron catalysts for a zinc-air battery and hydrogen-air fuel cell. *Nat Commun*, 2018, 9: 5422
- 43 Du D, Zhao S, Zhu Z, *et al.* Photo-excited oxygen reduction and oxygen evolution reactions enable a high-performance Zn-air battery. *Angew Chem Int Ed*, 2020, 59: 18140–18144

**Acknowledgements** This work was financially supported by the National Natural Science Foundation of China (21601137, 51972238, U21A2081, and 22105147), the Basic Science and Technology Research Project of Wenzhou, Zhejiang Province (G20190007), and the Special Basic Cooperative Research Programs of Yunnan Provincial Undergraduate Universities Association (202101BA070001-042).

**Author contributions** Qian J and Ge Y conceived the idea and supervised the project. Mao L contributed to the experiments. Chen D and Yang Y conducted the DFT calculations. Xu S and Xue J analyzed the results. The paper was written by Qian J and Mao L with contributions from Xiao K, Zhou X and Yang Z. All authors contributed to the general discussion.

**Conflict of interest** The authors declare that they have no conflict of interest.

**Supplementary information** Experimental details and supporting data are available in the online version of the paper.



**Lujiao Mao** received her Bachelor's degree from Jiaying Nanhu University in 2021, and now she is a graduate student at Wenzhou University. Her current research focuses on the design and synthesis of MOF-on-MOF-derived carbon nanomaterials for electrochemical applications.



**Jinjie Qian** is an associate professor at the College of Chemistry and Materials Engineering, Wenzhou University. He received his PhD degree from Fujian Institute of Research on the Structure, Chinese Academy of Sciences, under the guidance of Prof. Maochun Hong. His current research is mainly involved in the electrochemical research on carbon nanomaterials derived from MOFs for energy storage and conversion.

## 含有丰富铁物种的配体诱导中空MOF衍生碳纳米材料用于高效氧还原反应

毛璐娇, 葛勇杰\*, 陈丹丹, 杨远东, 徐少杰, 薛金航, 肖远远, 周学梅, 钱金杰\*, 杨植\*

**摘要** 合理地设计和制备低成本、高效、稳定的非贵金属基碳纳米材料具有重要意义。本文中我们在不同温度条件下, 通过有机配体交换将MOF-5转换为ZIF-8, 其过程中可以捕捉到ZIF-8的中间态(ZIF-8-M)并得到最终态(ZIF-8-F)。将掺杂Fe离子的MOF材料进行热解后, 得到的Fe-ZIF-8-F-900材料具有大的比表面积、高的石墨化程度、丰富的碳纳米管以及高活性的铁物种等优点。这些特性有助于后续氧还原反应(ORR)更好的电子转移和质量传输。与Pt/C相比, Fe-ZIF-8-F-900具有优异的ORR性能, 如较正的起始电位(0.982 V), 大的极限电流密度(5.41 mA cm<sup>-2</sup>)和较小的Tafel斜率(40.6 mV dec<sup>-1</sup>), 且在10小时后电流保持率仍高达94.4%。此外, 实验和理论结果均证实了Fe-ZIF-8-F-900组装的锌空气电池在实际应用中表现优异。本研究将为高效、低成本的非贵金属基电催化剂的开发和制备提供合理的设计策略, 并为其在能源相关领域的实际应用指明方向。